

Journal of Materials Chemistry A

Accepted Manuscript



This is an *Accepted Manuscript*, which has been through the Royal Society of Chemistry peer review process and has been accepted for publication.

Accepted Manuscripts are published online shortly after acceptance, before technical editing, formatting and proof reading. Using this free service, authors can make their results available to the community, in citable form, before we publish the edited article. We will replace this *Accepted Manuscript* with the edited and formatted *Advance Article* as soon as it is available.

You can find more information about *Accepted Manuscripts* in the [Information for Authors](#).

Please note that technical editing may introduce minor changes to the text and/or graphics, which may alter content. The journal's standard [Terms & Conditions](#) and the [Ethical guidelines](#) still apply. In no event shall the Royal Society of Chemistry be held responsible for any errors or omissions in this *Accepted Manuscript* or any consequences arising from the use of any information it contains.

ARTICLE

C-axis Preferentially Oriented and Fully Activated TiO₂ Nanotube Arrays for Lithium Ion Batteries and Supercapacitors

Cite this: DOI:
10.1039/x0xx00000x

Received 00th January 2012,
Accepted 00th January 2012

DOI: 10.1039/x0xx00000x

www.rsc.org/

Dengyu Pan,^{*a} He Huang,^b Xueyuan Wang,^a Liang Wang,^a Haobo Liao,^a Zhen Li,^{*b} and Minghong Wu^{*c}

We report the fabrication of long titanium dioxide nanotube arrays with highly *c*-axis preferentially oriented crystallization and a high concentration of oxygen vacancies by second anodization in ethylene glycol and annealing under poor-oxygen conditions. By optimizing growth and annealing conditions, the [001] oriented crystallization is maximized, and 31.7% of the total Ti ions exists as Ti³⁺ states. The carrier density of the [001]-oriented TiO₂ nanotube arrays is two orders of magnitude higher than that of the randomly oriented TiO₂ nanotube arrays. The unusual *c*-textured crystallization confined within nanotubes may involve the formation of TiO₆²⁻ octahedrons with a gradient distribution along the tube axis, preferential nucleation at the top, and preferential growth downwards along the *c* axis. Because of the *c*-axis preferential orientation and a high-concentration of oxygen vacancies, long TiO₂ nanotube arrays can serve as superior electrodes for both lithium ion batteries and supercapacitors without addition of any conductive agents. Long *c*-oriented TiO₂ nanotube arrays deliver reversible capacities of 293 mA h g⁻¹ at 0.5 C and 174 mA h g⁻¹ at 5C with Coulombic efficiencies over 99%, and hold areal capacitance of 8.21 mF cm⁻² with an 85% capacitance retention after 5000 cycles. Double roles played by oxygen vacancies are identified in increasing electrical conductivity and activating the rich-Li phase.

Introduction

Lithium ion batteries (LIBs) and supercapacitors with high energy and power densities are urgently required for developing electric and/or hybrid vehicles. To increase energy densities, electrode materials with high specific capacities (e.g. Sn- and Si-based LIBs)¹ or specific capacitances (e.g. MnO₂- and RuO₂-based pseudocapacitors)^{2,3} have been developed. However, electrodes made of highly active materials commonly suffer from low Coulombic efficiencies, poor cycling stability, low rate capabilities, and safety concerns, which limit their practical applications in LIBs and supercapacitors. These issues are largely ascribed to the exceptionally large structural deformation during ion insertion/extraction processes, which leads to partial interruption of established electron transport and ion diffusion pathways. In this context, it is of crucial importance to establish durable highways for electron transport and ion diffusion in electrodes.

Recently, TiO₂ and derivatives (Li-Ti-O, Na-Ti-O, and H-Ti-O systems) as nearly zero-strain active materials have drawn increasing interest for electrochemical energy storage.⁴⁻²¹ Although a rich-Li phase (TiO₂Li_{0.5}) forms during lithium insertion, the whole structure keeps stable in extended cycling with a negligible volume change of only 4%.⁵ Moreover, Ti-based LIBs with a high Li-insertion potential can achieve safer

operation than C-, Sn, and Si-based LIBs by avoiding the formation of lithium dendrites.⁴ Unfortunately, Ti-based anode materials are electrical insulators (Li-Ti-O, Na-Ti-O, and H-Ti-O) or less conductive wide-bandgap semiconductors (TiO₂). As a result, they themselves cannot provide direct electron transport highways for driving the electrochemical process. An effective common strategy is to fabricate composite anodes using porous particles, thin sheets, or thin nanowires/nanotubes as the active material mixed with necessary additives of insulating binder and conductive agent to enhance their mechanical strength and electrical conductivity.⁴⁻¹⁰ However, such electron and ion diffusion pathways are easily blocked by inhomogeneous mixture and poor physical contact between the active material and the current collector. Moreover, overall specific capacities are substantially reduced owing to the incorporation of inactive additives in large amounts. To overcome these limitations from composite anodes, one-dimensional (1D) TiO₂ arrays directly grown on current collectors have been suggested to serve as additive-free anodes.¹¹⁻¹⁸ Recently, almost all efforts have focused on the fabrication of TiO₂ 1D arrays in the anatase phase because this phase has superior photoelectronic conversion^{19,20} and electrochemical energy storage^{11,12,14-18,21} properties to other polymorphs. However, anatase TiO₂ 1D arrays reported so far are polycrystalline and randomly oriented.^{11,12,14-18,21} These

randomly oriented 1D arrays show good Li storage properties only when 1D lengths are limited to few micrometers (generally smaller than 2 μm).^{11-17,21} If these arrays are elongated to more than 10 μm to increase areal capacity, a large fraction of arrays becomes “dead” because electrons from current collectors cannot be transported to a long enough vertical distance owing to frequent electronic scattering by rich crystal interfaces.¹⁸ Because of this confinement, randomly oriented arrays can only be used in microbatteries to power microsensors and microactuators. For application in large batteries with high-density and high-power energy storage capacities, for example, to power vehicles, it is highly desirable to fabricate ultralong *c*-axis oriented (*c*-oriented) 1D arrays. Compared with randomly oriented arrays, *c*-oriented TiO₂ 1D arrays with the *c*-axis perpendicular to current collectors can provide much longer electron diffusion lengths (hundreds of micrometers versus few micrometers)²² and shorter, straighter electron pathways from current collectors to active sites. Moreover, *c*-oriented 1D arrays also provide more efficient lithium ion diffusion pathways along the *c* axis.⁸ Therefore, *c*-oriented anatase TiO₂ 1D arrays are expected to keep excellent lithium storage properties even when elongated to hundreds of micrometers.

Among TiO₂ 1D arrays, anodized TiO₂ nanotube arrays (TNAs) have drawn the most attention for various applications, such as solar cells,^{19,20,23} LIBs,^{11,12,14-18} and supercapacitors.²⁴⁻²⁸ Their geometric sizes such as tube length, diameter, and wall thickness can be tuned easily by electrochemical parameters. Particularly, the use of organic electrolytes to replace aqueous electrolyte allows for the growth of ultralong TNAs with tube length up to few hundreds of micrometers.¹⁸⁻²⁰ However, as-anodized TNAs are amorphous, and further annealing treatment can only produce polycrystalline and randomly oriented TNAs (r-TNAs). Here, we report for the first time a simple method for transforming long amorphous TNAs anodized in ethylene glycol into highly *c*-oriented anatase TNAs (*c*-TNAs) by poor-oxygen annealing. We found that annealing under poor-oxygen conditions not only activates TNAs by introducing a high concentration of oxygen vacancies and electronic carriers, but also creates fast and durable highways for electrons and ions (Li⁺ and H⁺ ions) by *c*-axis preferentially oriented (*c*-textured) crystallization. The mechanism of the unusual *c*-textured crystallization confined within nanotubes is proposed. We further show that *c*-TNAs fully activated by a high concentration of oxygen vacancies are superior to r-TNAs deactivated by rich-oxygen annealing for applications in LIBs and supercapacitors. We also discuss key roles played by oxygen vacancies in constructing the highly conducting pathway and promoting the phase transition of the rich-Li phase.

Results and discussion

Fig. 1 shows the XRD patterns of r- and c-TNAs grown on Ti foils by second anodic oxidation in ethylene glycol containing 2 wt% H₂O and annealed at 450 °C in rich-oxygen (air) and poor-oxygen (vacuum) atmospheres, respectively. The r-TNAs show diffraction characteristics of polycrystalline anatase TiO₂ powder, with the (101) diffraction peak the strongest. Like previous reports,^{11,12,14-20} the r-TNAs show random crystallographic orientation during the thermal crystallization under the rich-oxygen conditions. However, under poor-oxygen annealing conditions, the same anodized TNAs show highly oriented crystallization or texturing in the [001] direction perpendicular to the substrates. Compared with

the XRD pattern of the r-TNA sample, the (004) peak of the *c*-TNA sample is significantly enhanced and becomes the strongest, whereas the strongest (101) peak becomes as weak as (200) and (105) peaks.

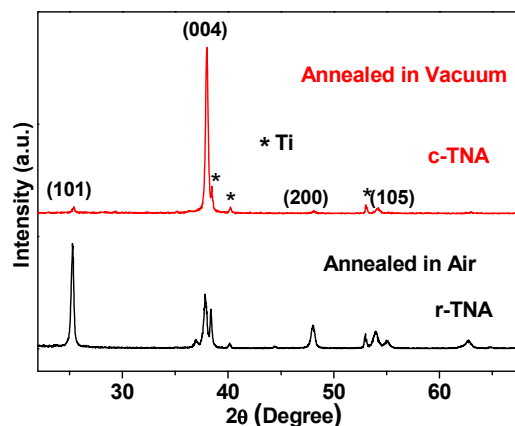


Figure 1. XRD patterns of r- and c-TNAs

Fig. 2a shows a large-area top view of the *c*-TNAs with uniform and smooth surface. As previously reported,¹⁹ the TNAs grown by second anodization have a higher quality than those by once anodization owing to the presence of hexagonally packed patterns made of regular shallow pits formed by removal of the first-grown TNAs. The ordered patterns serve as templates to guide the vertical growth of nanotubes underneath during the second oxidation, and finally evolve into a mesoporous top layer with pore diameters of ~ 120 nm (Fig. 2b). The rigid template effectively buffers the stress formed during the growth and subsequent annealing processes, and thus avoids the formation of debris and cracks on the surface. Beneath the porous layer, the opening of nanotubes with inner diameter of ~ 90 nm can be observed. The lateral view of the array (the inset in Fig. 2a) shows that the nanotubes are grown vertically from bottom to top with length of 15.5 μm . Fig. 2c shows the TEM image of a single nanotube segment from the array. TEM EDS analysis reveals a gradient distribution of Ti/O atomic ratio along the tube axis: the oxygen content gradually decreases from one end to another. Its magnified view (Fig. 2d) shows that there are short protrusions sparsely grown on the outer wall. The HRTEM image of the wall near a protrusion (Fig. 2e) shows a two-dimensional crystal lattice composed of (004) and (112) planes of anatase TiO₂ at an angle of 61° with a spacing of 0.238 and 0.233 nm, respectively. The (004) planes are perpendicular to the [001] growth direction. The fast Fourier transform (FFT) pattern of the lattice (insets of Fig. 2e) shows a single-crystal-like pattern with a crystallographic zone axis of [1-10]. The two-dimensional crystal lattice also extends into the protrusion. Near another protrusion pointing at another direction, the HRTEM image of the wall shows a two-dimensional crystal lattice composed of (101) and (040) planes with a spacing of 0.252 and 0.235 nm, respectively. The FFT pattern also shows a single-crystalline nature with a crystallographic zone axis of [10-1]. The TEM observation of r-TNAs is shown in Fig. S1 (Supporting Information). A SAED pattern of a fragment from the r-TNA shows polycrystalline diffraction rings of (101), (004), and (200) planes (Fig. S1a, b). The HRTEM image (Fig. S1c) reveals that the nanotubes consist of anatase TiO₂ crystallites with random crystallographic orientation.

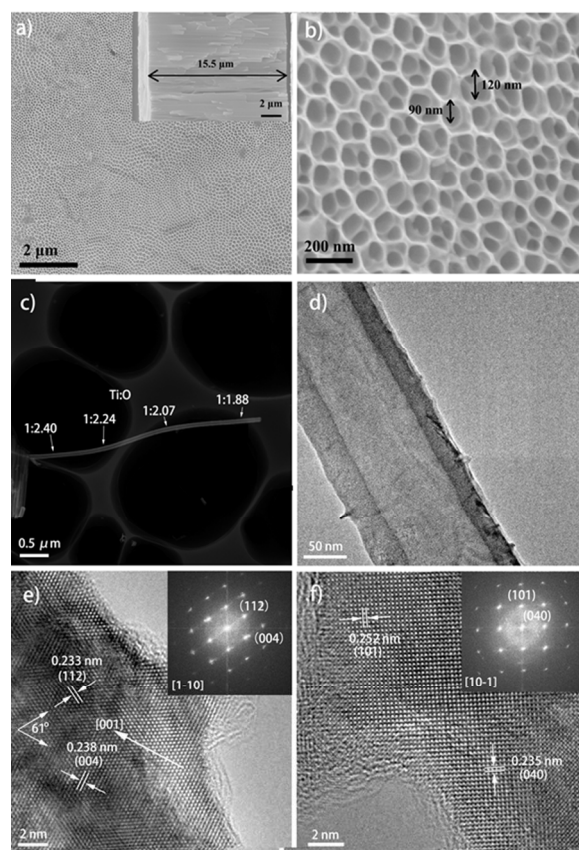


Figure 2. SEM (a-b) and TEM (c-f) images of the c-TNA. (a) Top and lateral (the inset) images of the array; (b) Magnified top view; (c) EDS analysis on the distribution of Ti/O atomic ratio along the axis of a single TiO₂ nanotube from the TNA; (d) Magnified image of the nanotube; (e) HRTEM image of the nanotube wall along [1-10] crystallographic zone axis; (f) HRTEM image of the wall along [10-1] zone axis

Table 1. Effects of anodic oxidation conditions (water content and growth time) and annealing atmosphere on nanotube length and crystallization orientation (I_{004}/I_{101} ratio) of TNAs.

Water content (wt%)	Growth time (h)	Annealing atmosphere	Nanotube length (μm)	I_{004}/I_{101} ratio
2	2	Air	15.5	0.5
2	2	O ₂	15.5	1.2
2	2	Ar	15.5	20.3
2	2	Vacuum	15.5	23.2
2	8	Vacuum	38.0	38.3
3	2	Vacuum	12.1	2.7
4	2	Vacuum	6.6	1.4
1	2	Vacuum	8.9	3.8

In order to systematically investigate the unusual *c*-textured crystallization phenomenon, we prepared a series of TNA samples by varying anodic oxidation parameters (water content and growth time) and annealing atmosphere. The XRD intensity ratio of I_{004}/I_{101} in these samples (XRD patterns in Fig. S2 and S3) is used to evaluate the [001] texturing level. Table 1 summarizes the effects of these anodic oxidation and annealing

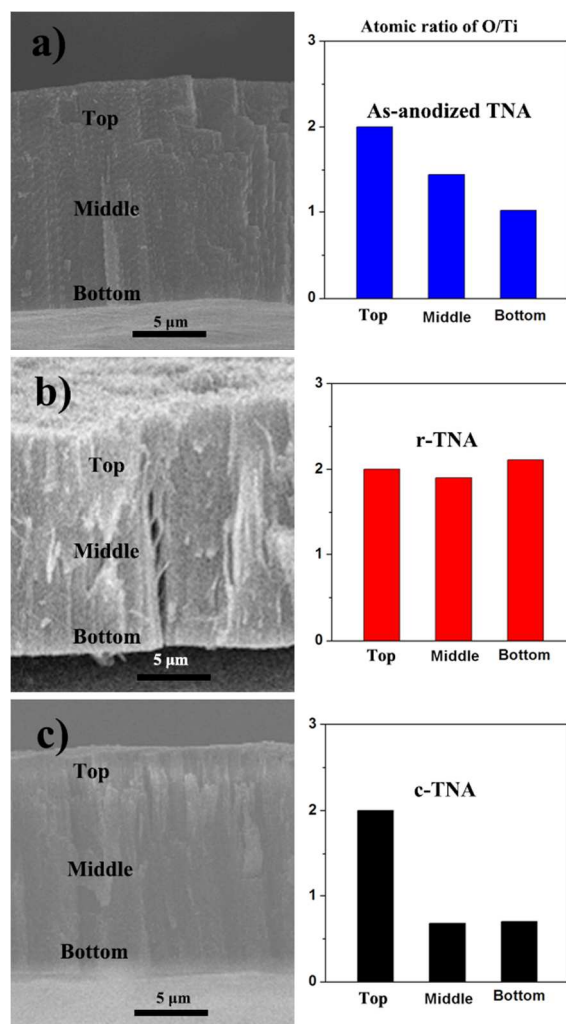


Figure 3. Qualitative analysis on the O/Ti atomic ratio for as-anodized amorphous TNA (a), air-annealed r-TNA (b), and vacuum-annealed c-TNAs at top, middle, and bottom sites using EDS in SEM.

conditions on [001] texturing and tube length. We found that annealing in a poor oxygen atmosphere such as vacuum ($<10^{-1}$ Pa) or Ar gas is the most crucial factor to drive the [001] texturing. Under the same anodic oxidation conditions (water content of 2 wt %; growth time of 2 h), vacuum or Ar annealing produces [001] textured TNAs with I_{004}/I_{101} as high as 20-23. When growth time increases to 8 h, the nanotube length increases from 15.5 to 38.0 μm, and the ratio of I_{004}/I_{101} increases from 20.3 to 38.3. Further prolonging growth time can no longer increase the texturing level because the surface of the array is covered with disordered debris (Fig. S4). In contrast, upon rich oxygen annealing (air or pure O₂ gas) under the otherwise same conditions, the ratio of I_{004}/I_{101} is reduced to only 0.5-1.2. Particularly for the air-annealing, the intensity of (101) is instead higher than that of (004), revealing that both moisture and oxygen in air suppress the textured crystallization. Besides the annealing atmosphere, water content in the electrolyte also requires careful regulation prior to the annealing. Under the same growth time (2 h) and vacuum-annealing conditions, a slight variation in water content around 2 wt % can exert a great effect on the oriented crystallization. To maximize the oriented crystallization, the optimum water

content is 2 wt %. When the content is deviated from 2 wt %, the ratio of I_{004}/I_{101} decreases dramatically, though TNAs are also annealed in the poor oxygen atmosphere. Thus we can identify two indispensable control parameters—exactly tuned water content in an organic electrolyte and poor-oxygen annealing for the oriented crystallization.

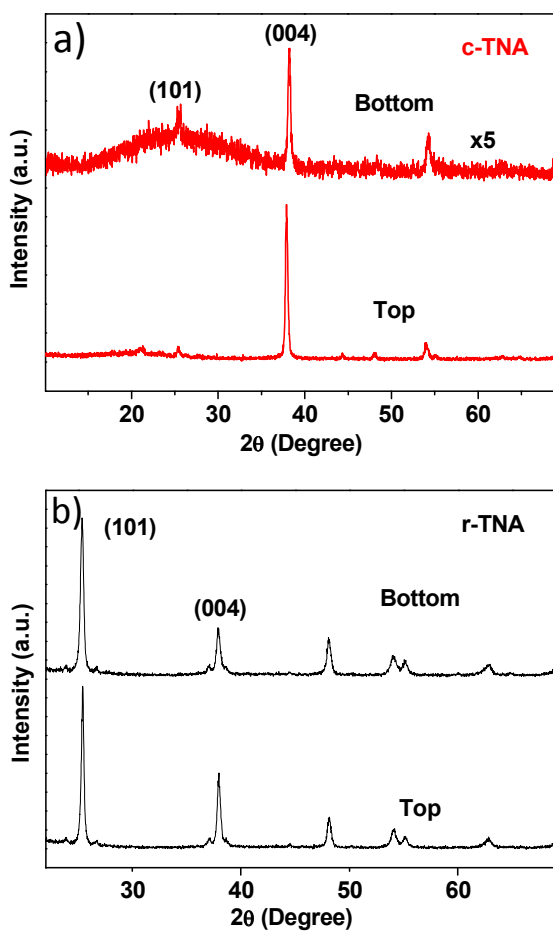
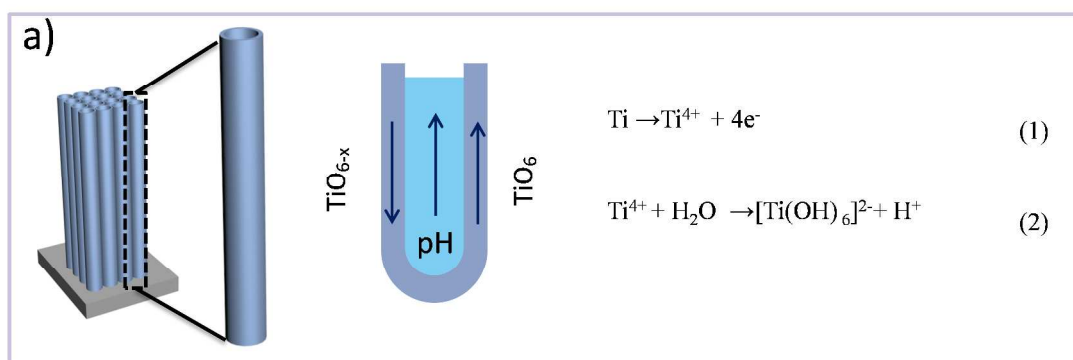


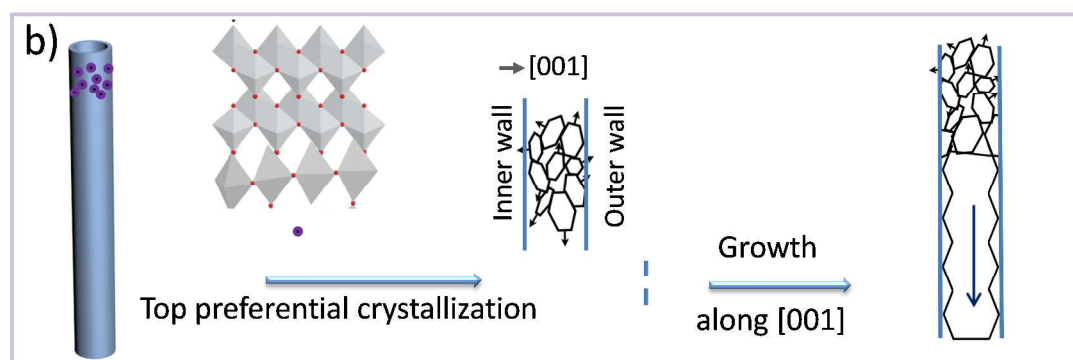
Figure 4. XRD patterns of c-TNAs (a) and r-TNAs (b) exfoliated from the Ti substrates measured from top and bottom sides.

We now discuss the possible mechanism of the *c*-textured crystallization induced by poor-oxygen annealing. As we know, TiO_6^{2-} octahedrons are basic building blocks for both amorphous and crystalline (anatase, rutile, and brookite) TiO_2 polymorphs, depending on arrangement manners of the units.²⁵ For the amorphous TNAs, TiO_6^{2-} octahedrons are produced by full hydrolysis of Ti^{4+} ions formed by anodization of metal Ti at the solid-liquid interface, as shown in equations (1) and (2) (Scheme 1a). Because the anodization occurs in the F-containing electrolyte, $[\text{TiO}_{6-x}\text{F}_x]^{2-}$ octahedrons are also incorporated into the amorphous TNAs.³⁰ F-doped Ti-O octahedrons can be further converted into TiO_6^{2-} octahedrons when pH is high enough. Recently, the establishment of a pH profile localized within nanotubes has been proposed to be crucial to the formation of TNAs.³¹ According to this mechanism, HF is created at the bottom of nanotubes as an etching agent to form pores, whereas at sites away from the acidic region, such as upper sites of nanotubes, higher pH values are established as a result of migration and diffusion

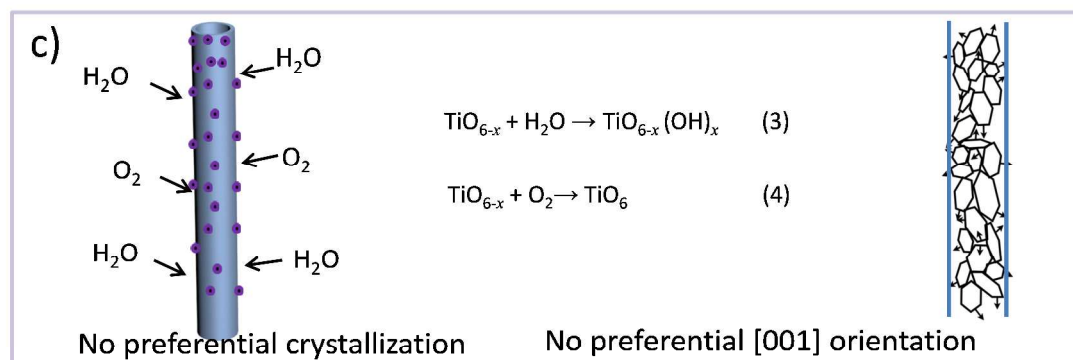
effects of the pH buffer species (NH_4F). The establishment of the pH profile with a large gradient is key to the formation of long TNAs. The pH gradient is strongly dependent on water content. In an extreme case, such as anodization in an aqueous HF based electrolyte, the pH gradient is small, so very short TNAs only several hundreds of nanometers in length can be grown.^{11, 12, 14-17} In the ethylene glycol electrolyte, the length of TNAs is strongly dependent on water content. With other conditions unvaried, the largest nanotube length occurs at a water content of 2 wt % (Table 1, Fig. S5), suggesting that there is the largest pH gradient in the case of 2 wt % water. By coincidence, the optimum water content for maximizing the oriented crystallization is also 2 wt %. These unexpected consistent results suggest that the establishment of the pH profile with a large gradient is also key to the oriented crystallization. We further propose that the gradient distribution of pH along the tube axis leads to a gradient distribution of the content of TiO_6^{2-} octahedrons: Larger the pH value at upper sites of nanotubes is, higher the content of TiO_6^{2-} octahedrons is (Scheme 1a). To confirm this gradient distribution, SEM-based EDS analysis on the amorphous TNAs was performed. Although EDS analysis on the chemical composition of nanomaterials has a much lower precision than other surface analysis techniques (XPS and Rutherford backscattering spectroscopy (RBS)), we can qualitatively investigate the distribution of the O/Ti atomic ratio along the tube axis using this technique. The O/Ti atomic ratio was found to gradually decrease from top to bottom (Fig. 3a), suggesting that the content of TiO_6^{2-} octahedrons also decreases from top to bottom (In other words, the content of $[\text{TiO}_{6-x}\text{F}_x]^{2-}$ octahedrons gradually increases from top to bottom). In a previous study, Berger and coworkers used more accurate RBS technique to determine the average composition of amorphous TNAs grown under the same anodization conditions as ours.³⁰ The average O: Ti: F atomic ratio of 1.69: 1: 0.48 reveals deficient oxygen content and the presence of F element. The deficient oxygen content of the amorphous TNAs at sites from middle to bottom is fully supplemented upon annealing in air by reactions of (3) and (4) (Fig. 3b), but further decreases by vacuum reduction at 450 °C (Fig. 3c). The gradient distribution of TiO_6^{2-} building units exerts substantial effects on the crystallization of TNAs. Upon annealing under poor-oxygen conditions at 450 °C, TiO_2 nucleus form preferentially at the top, where TiO_6^{2-} octahedrons with a high enough concentration rearrange into the anatase phase (Scheme 1b). Nanocrystals enclosed by exposed {004} and {101} facets grow in the preferential [001] direction, forming a thin mesoporous layer composed of nanocrystals with random [001] orientations. As the crystallization proceeds, only nanocrystals with the [001] orientation downwards and parallel to the tube axis are able to continue to grow in the [001] direction while the growth of all other nanocrystals with the [001] orientation deviating the axis is finally confined within the 10-nm-thickness walls. As a result, the continuous unconfined axis growth leads to the highly *c*-textured crystallization. For annealing under rich-oxygen conditions (Scheme 1c), however, the gradient distribution of TiO_6^{2-} octahedrons along the axis is broken up rapidly by enough oxygen incorporation from H_2O and O_2 in air, and a uniform distribution of TiO_6^{2-} octahedrons is established. Therefore, identical nucleation and growth for any sites occur, eventually producing anatase nanocrystals with [001] towards any directions. To further examine the crystallization of TNAs under poor-oxygen annealing conditions, we compare the XRD patterns of the fully-exfoliated vacuum-annealed TNA films



As-anodized TNA



Highly [001] oriented TNA



Randomly oriented TNA

Scheme 1. Schematic diagram showing two different crystallization processes of amorphous TNAs annealed in different atmospheres. (a) As-anodized TNAs by anodic oxidation of Ti foil in ethylene glycol containing 2 wt% of H₂O. Two arrows in the wall indicate different content distributions of TiO₆ and TiO_{6-x} along the tube axis. An arrow in the electrolyte indicates pH profile with a gradient distribution. (b) [001] preferentially oriented crystallization induced by annealing in vacuum. The process involves (1) the formation of anatase crystal nucleus (purple dots made of ordered TiO₆ octahedrons) preferentially nucleated at the top, where the octahedrons have a high enough concentration, and (2) crystal growth preferentially in the [001] direction as shown by arrows, thus forming anatase nanocrystals enclosed by exposed {004} and {101} facets. Among these nanocrystals, only one crystal with the [001] direction along the tube axis continues to grow, whereas the growth of others with the [001] direction deviating the axis is stopped owing to the confinement by the inner and outer walls. (c) Randomly oriented crystallization induced by annealing in air. First, low-coordinated TiO_{6-x} reacts with H₂O and O₂ in air, providing a great number of TiO₆ and TiO_{6-x}(OH)_x octahedrons for subsequent crystal nucleation and growth at random sites. As a result, identical nucleation and growth for any sites occur, producing anatase nanocrystals with [001] towards any directions.

with top and bottom surfaces directly exposed to the X-ray beam (Fig. 4a). Different from the highly (004)-oriented XRD pattern from the top, the bottom shows a wide diffraction band at 25° characteristic of an amorphous state. This result indicates that the upper section of amorphous TNAs is well crystallized into single-crystalline-like, [001] oriented 1D arrays whereas the bottom section keeps the amorphous state though annealing temperature is high enough. This unusual site-dependent crystallization phenomenon is consistent with the gradient distribution of the content of TiO_6^{2-} octahedrons in the as-anodized TNAs. Because the content of TiO_6^{2-} octahedrons at the bottom is far too low, the re-arrangement of the octahedrons into the anatase phase is frustrated. However, under air annealing conditions, a uniform distribution of TiO_6^{2-} octahedrons is established rapidly, so annealing in air does not induce any site-dependent crystallization. As shown in Fig. 4b, the XRD patterns of the fully-exfoliated r-TNA films with top and bottom surfaces directly exposed to the X-ray beam show the same polycrystalline diffraction pattern.

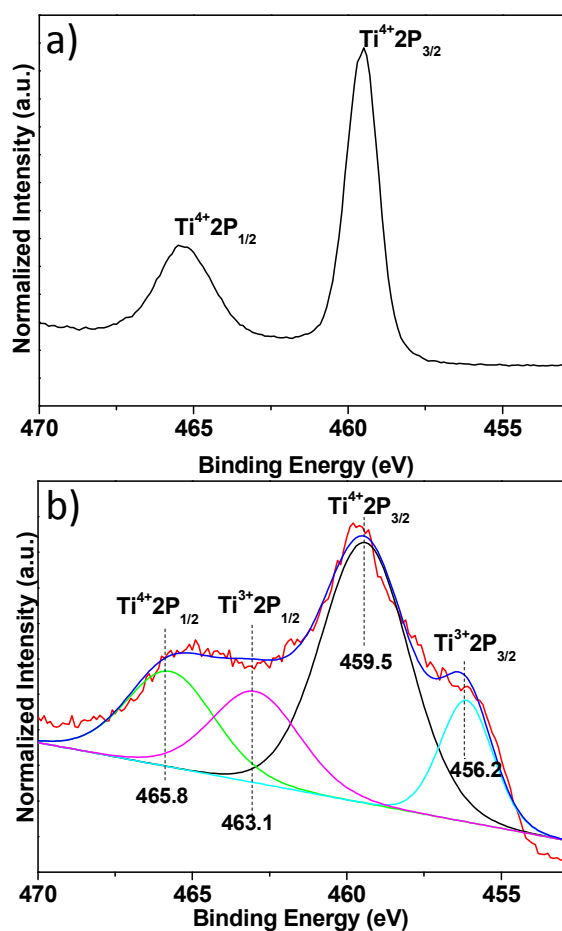


Figure 5. Ti 2p core-level XPS spectra of r-TNAs (a) and c-TNAs (b). The spectrum of c-TNAs is fitted well into four peaks of $\text{Ti}^{4+} 2\text{p}_{1/2}$, $\text{Ti}^{3+} 2\text{p}_{1/2}$, $\text{Ti}^{4+} 2\text{p}_{3/2}$, and $\text{Ti}^{3+} 2\text{p}_{3/2}$ centered at ~ 465.1 , 458.8 , 456.2 , and 455.4 eV.

Fig. 5 shows the Ti 2p core-level XPS spectra of the r- and c-TNAs. In the spectrum of the r-TNAs (Fig. 5a), the symmetric Ti 2p peaks indicate stoichiometric TiO_2 with a very low concentration of defects because of the annealing under rich-oxygen conditions. In the spectrum of the c-TNAs (Fig. 5b), a new well-resolved Ti 2p peak appears at 456.2 eV with a

3.3 eV shift to lower binding energy. This new peak can be ascribed to $\text{Ti}^{3+} 2\text{p}_{3/2}$ (involving the formation of oxygen vacancies).⁷ The peak of $\text{Ti}^{3+} 2\text{p}_{1/2}$ can be obtained at 463.1 eV by fitting, with a redshift of 2.7 eV relative to the state of $\text{Ti}^{4+} 2\text{p}_{1/2}$. The content of oxygen vacancies or Ti^{3+} ions can be estimated to be about 31.7% of the total Ti ions from the signal intensity ratio of $\text{Ti}^{3+} : (\text{Ti}^{4+} + \text{Ti}^{3+})$, indicating of the formation of a high concentration of oxygen vacancies owing to the deficient oxygen content of the amorphous TNAs and the poor-oxygen annealing.

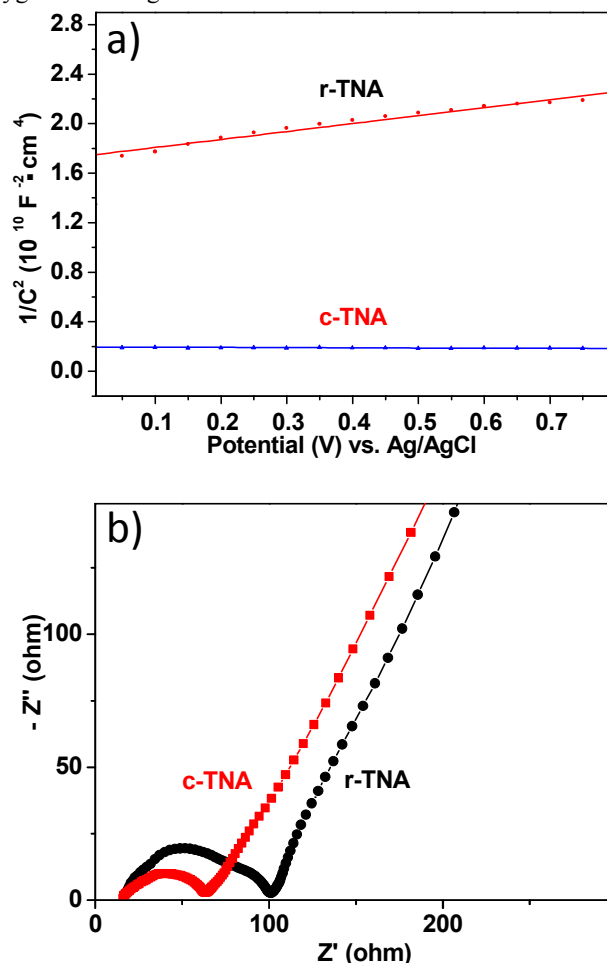
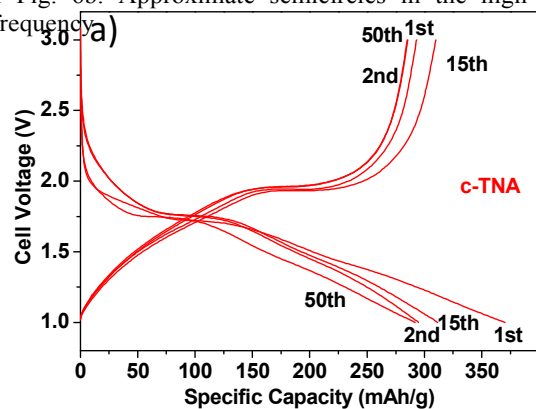


Figure 6. Mott-Schottky plots (a) and Nyquist plots (b) of the c- and r-TNAs.

To investigate the effect of annealing on the electrical properties of TNAs, electrochemical impedance measurements were conducted on the c-TNA and r-TNA samples. Fig. 6a shows Mott-Schottky plots derived from the electrochemical impedance at each potential with 10 kHz frequency in the dark.²⁴ The two Mott-Schottky plots exhibit a positive slope, indicating n-type semiconductor character. Based on the Mott-Schottky equation,²⁴ the carrier densities of the samples are calculated. The carrier density of the c-TNAs is as high as $2.62 \times 10^{23} \text{ cm}^{-3}$, two orders of magnitude higher than that of the r-TNAs ($2.17 \times 10^{21} \text{ cm}^{-3}$). The high carrier density of the c-TNAs is ascribed to the high concentration of oxygen vacancies, which are known to be intrinsic electron donors in TiO_2 . Their electrochemical impedance spectra measured in 1M LiPF_6 and presented in the form of Nyquist plots are

shown in Fig. 6b. Approximate semicircles in the high-to-medium frequency



is necessary to activate TiO_2 1D arrays by introducing a great number of oxygen vacancies to the particle interior. However,

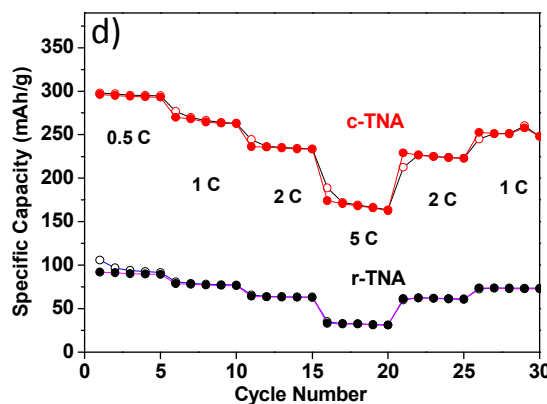
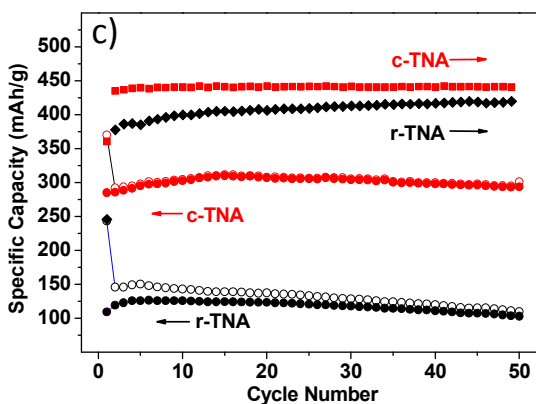
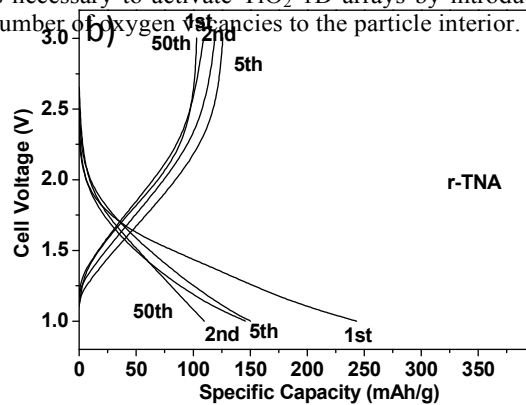


Figure 7. (a) Charge/discharge curves of c-TNAs. (b) Charge/discharge profiles of r-TNAs. (c) Discharge/charge capacities and Coulombic efficiencies of the two samples versus cycle number at a rate of 0.5 C. (d) Rate capacities of the arrays as a function of cycle number.

range correspond to a charge-transfer process and the charge-transfer resistance can be estimated from the difference between the left and right intercepts with the Z' axis.¹⁴ The c-TNAs have a smaller charge-transfer resistance of 48.5Ω than that of the r-TNAs (84.5Ω), which can be ascribed to the high concentration of oxygen vacancies, longer electron diffusion lengths, and shorter, straighter electron pathways. The bulk resistance largely resulting from a junction barrier potential between TiO_2 and metal Ti can also be estimated from the left intercept. The two samples show nearly identical bulk resistance of 18Ω because of the similar TiO_2 -Ti junction.

A deep understanding of the Li-ion insertion mechanism into TiO_2 is of prime importance for improving the storage performances of Ti-based LIBs. Previous experimental studies on TiO_2 anodes have identified the formation of poor-Li and rich-Li phases during the lithium insertion process.⁶ Accompanying the formation of these Li-insertion phases, a high concentration of Ti^{3+} ions is created.⁷ The formation of Ti^{3+} ions implies the creation of oxygen vacancies. In other words, to facilitate the formation of the rich-Li phases, oxygen ions near active sites require fast diffusion to nearby sites such as surface sites or existing oxygen vacancies. Researchers have proposed simultaneous Li^+ and O^{2-} diffusion creating oxygen vacancies and surface transition metal migration.^{32,33} For lithium insertion into the interior of TiO_2 1D arrays, if no rich oxygen vacancies exist in the interior, the rich-lithium phase is difficult to form because oxygen ions in the interior are difficult to diffuse to particle surface at room temperature. Therefore, it

the evidence for the activation of the rich-lithium phase ($\text{TiO}_2\text{Li}_{0.5}$) by oxygen vacancies is lacked. Here, we present this evidence by investigating the lithium storage properties of two typical TNA samples with few oxygen vacancies (r-TNAs) and with a high concentration of oxygen vacancies (c-TNAs). Fig. 7a shows the voltage profiles of the c-TNA anodes measured in the voltage range of 1-3 V vs Li/Li^+ at a rate of 0.5 C for several typical cycles. The discharge voltage profiles are similar to those of anatase TiO_2 anodes, consisting of three typical voltage regions A, B, and C.⁶ The region A shows a steep voltage drop from 3.0 to 1.75 V vs Li/Li^+ , corresponding to lithium insertion into the poor-Li tetragonal anatase lattice (TiO_2Li_x , $x = 0.03$ -0.12). The region B is a plateau at a potential of 1.75 V vs Li/Li^+ , ascribed to the Li insertion into the typical orthorhombic rich-Li phase of $\text{TiO}_2\text{Li}_{0.5}$. The region C is the voltage tail at a potential from 1.75 to 1.0 V vs Li/Li^+ , involving the lithium insertion into the complex surface or interface regions because the smaller the anatase crystallite size, the longer this region is. For the sample r-TNA (Fig. 7b), in contrast, the discharge voltage profiles show only two regions A and C without the plateau B. The deactivation of the lithium insertion into the common rich-Li phase of $\text{TiO}_2\text{Li}_{0.5}$ at region B in the air-annealed r-TNA with few oxygen vacancies provides clear evidence for the activation of the rich-Li phase by oxygen vacancies. This contrast demonstrates that the introduction of high-concentrated oxygen vacancies not only provides a high carrier concentration for increasing electrical

conductivity but also activates the formation of the rich-Li phase.

In contrast, the discharge and charge capacities at the 1st cycle are only 243, 109 mA h g⁻¹, respectively. The reversible capacity (109 mA h g⁻¹) is even smaller than the theoretical

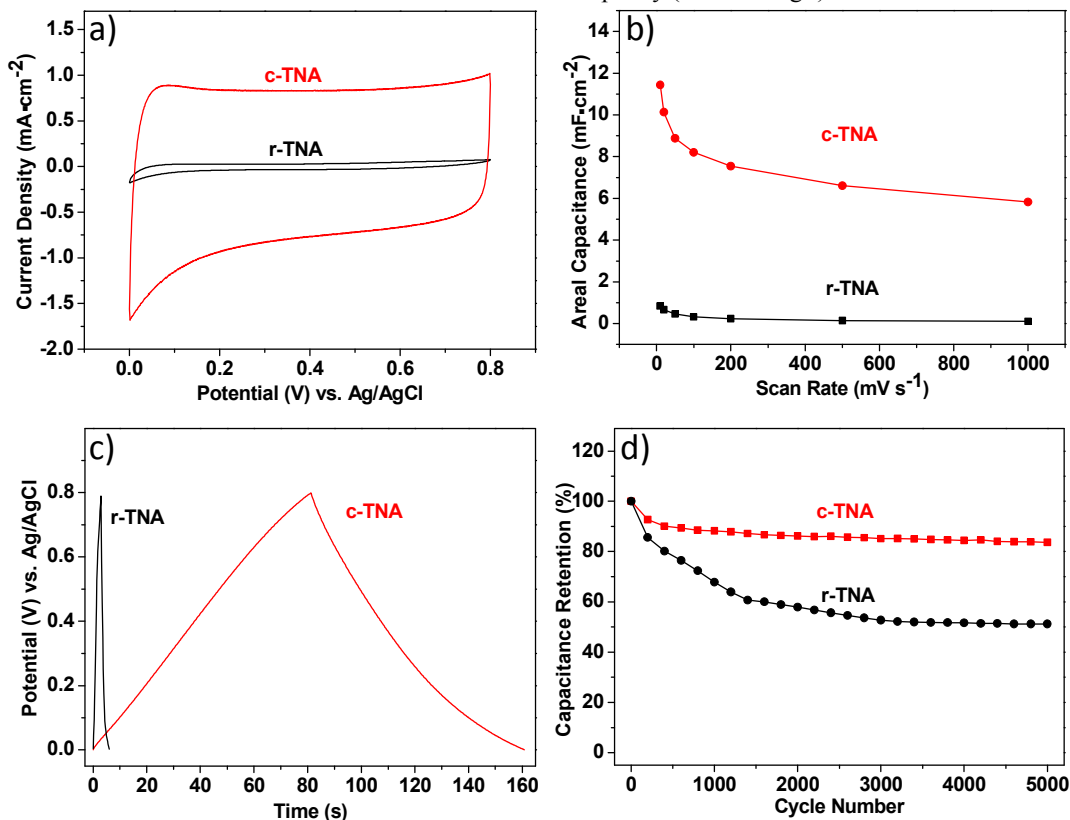


Figure 8. (a) CV curves of the c- and r-TNAs obtained at a scan rate of 100 mV s⁻¹. (b) Their areal capacitance at different scan rates. (c) Galvanostatic charge/discharge curves collected at a current density of 100 μA cm⁻². (d) Cycle performances at a scan rate of 100 mV s⁻¹ for 5000 cycles.

The lithium storage performances of the c- and r-TNAs on Ti substrates are evaluated by specific capacity. For the c-TNAs, the discharge and charge capacities of the first cycle at a rate of 0.5 C are 370, 293 mA h g⁻¹, respectively (Fig. 7a). Their cycle performances are also evaluated. As shown in Fig. 7c, the c-TNAs show excellent cycle stability. The Coulombic efficiencies from the second to the 50th cycle keep over 99% except the relative small value of 77% at the first cycle. With increasing cycling number, the reversible capacity (charge capacity) slowly increases to 310 mA h g⁻¹ at the 15th cycle with a notable increase of 17 mA h g⁻¹. As shown in Fig. 7a, the charge curve of the 15th cycle is on the right of those of the 2nd and 1st cycles. The increased reversible capacity occurring in the electrochemical process can be ascribed to electrochemical activation by oxygen vacancies formed *in situ*.³⁴ After 50 cycles, the reversible capacity remains as high as 286 mA h g⁻¹, corresponding to the lithium insertion into TiO₂Li_{0.9}, much higher than the theoretical capacity (166.7 mA h/g) of bulk TiO₂ for 0.5 Li-ion insertion. To our knowledge, the long-term reversible capacity exhibited in the c-TNAs is the highest value reported so far among all Ti-based anodes of TiO₂ polymorphs and derivatives (Li-Ti-O, Na-Ti-O, and H-Ti-O systems) with capacities no more than 200 mA h/g.^{4, 5, 8-18} The c-TNAs also show high rate capacities (Fig. 7d). They deliver 270, 236, 174 mA h g⁻¹ at 1C, 2C, and 5C, respectively. For the r-TNAs,

capacity (166.7 mA h/g) of bulk TiO₂, mainly because of the deactivation of the rich-Li phase (TiO₂Li_{0.5}). Their Coulombic efficiency slowly increases from 44% at the first cycle to 93% at the 50th cycle, and rate capacities at 1C, 2C, and 5C are 79, 64, 33 mA h g⁻¹, respectively. Note that although the c- and r-TNAs have the same tube length, morphology, and anatase structure, the c-TNAs have superior Li storage performances to the r-TNAs, largely because the c-TNAs provide a high concentration of oxygen vacancies for dramatically increasing electrical conductivity and fully activating the formation of the rich-Li phase.³¹ Moreover, the c-TNAs create faster and durable highways for electrons and Li⁺ ions by *c*-axis preferentially oriented crystallization. Because of these microstructural optimization in crystal orientation and intrinsic defects (oxygen vacancies), the long c-TNAs (15.5 μm in length) are even superior to short 1D anatase arrays (≤2 μm in length) in lithium storage performances.¹¹⁻¹⁷ For example, 2-μm-long TNAs grown using arrays of ZnO nanorods as sacrificial template had capacities of 170, 160, and 140 mA h g⁻¹ at a rate of 1C, 2C, and 5C,¹¹ smaller than those of the c-TNAs (270, 236, 174 mA h g⁻¹ at 1C, 2C, and 5C). Our results suggest that ultralong 1D TiO₂ arrays can serve as superior additive-free anodes when they are grown or post-treated to induce *c*-axis preferential orientation and a high-concentration of oxygen vacancies. This structural design of highly *c*-oriented, fully activated, and

ultralong 1D oxide array anodes can overcome the difficulty in lithium insertion to active sites far away from current collectors.

The electrochemical capacitive properties of the *c*- and *r*-TNAs on the Ti substrates as working electrodes are also evaluated in a three-electrode H-shape electrochemical cell with a platinum wire counter electrode and an Ag/AgCl reference electrode in 0.5 M Na₂SO₄ solution. Fig. 8a shows the steady state cyclic voltammetric (CV) curves of the two electrodes collected at the scan rate of 100 mV s⁻¹. The CV curves exhibit rectangular shapes, indicating of their electrical double layer capacitive behavior. Fig. 8b shows the calculated areal capacitance of the two electrodes as a function of scan rate. The areal capacitance of the *c*-TNAs is much higher than that of the *r*-TNAs. At a scan rate of 100 mV s⁻¹, the *c*-TNA electrode has an areal capacitance of 8.21 mF cm⁻² with a 25 times enhancement compared to that of the *r*-TNA electrode (0.32 mF cm⁻²). The areal capacitance is the highest reported so far in TNA-based capacitors (0.1–0.9 mF cm⁻² in TNAs,^{25–28} 3.24 mF cm⁻² in hydrogenated TNAs²⁴). The *c*-TNA electrode also shows a good rate capacitance. When the scan rate increases from 10 to 1000 mV s⁻¹, the areal capacitance of the *c*-TNA electrode slowly falls from 11.44 to 5.83 mF cm⁻² with a good retention of 51% of the initial capacitance, whereas the *r*-TNA retains only 13% of the initial capacitance. Their electrochemical performances were further studied by galvanostatic charge/discharge measurements, as shown in Fig. 8c. The symmetric and prolonged charge/discharge curve of the *c*-TNA electrode reveals a good capacitive behavior. The areal capacitance of the *c*-TNA measured at a current density of 100 μA cm⁻² is calculated to be 10.08 mF cm⁻². Cycling stability tests at a scan rate of 100 mV s⁻¹ for 5000 cycles (Fig. 8d) show that the fully activated *c*-TNA has an excellent long-term cycling stability: the capacitance drops only ca. 16% after 5000 cycles. In contrast, for the deactivated *r*-TNA, the capacitance drops ca. 49% after 5000 cycles. The remarkable capacitive performance of the *c*-TNA electrode is ascribed to its enhanced electrical conductivity and fast H⁺ diffusion in the electrode.³⁴

Conclusions

We have achieved highly *c*-axis preferentially oriented crystallization and a high-concentration of oxygen vacancies in long TNAs by tuning water content in the anodization and poor-oxygen annealing in the crystallization. The *c*-textured crystallization confined within nanotubes may involve the formation of TiO₆²⁻ octahedrons with a gradient distribution along the tube axis, preferential nucleation at the top, and preferential growth downwards along the *c* axis. Under optimized water content (2 wt %) and poor-oxygen annealing atmosphere (vacuum), the ratio of I₀₀₄/I₁₀₁ is tuned to 38.3, and 31.7% of the total Ti ions exists as Ti³⁺ states. The carrier density of the *c*-oriented TNAs annealed in vacuum is two orders of magnitude higher than that of the random oriented TNAs annealed in air. Because of the *c*-axis preferential orientation and a high-concentration of oxygen vacancies, long TNAs can serve as superior electrodes for both lithium ion batteries and supercapacitors without addition of any conductive agents. Long *c*-oriented TNAs fully activated by oxygen vacancies deliver reversible capacities of 290 mA h g⁻¹ at 0.5 C and 170 mA h g⁻¹ at 5C with Coulombic efficiencies over 99%, and hold areal capacitance of 8.21 mF cm⁻² with a 85% capacitance retention after 5000 cycles. Moreover, the double roles played by oxygen vacancies in increasing

electrical conductivity and activating the rich-Li phase have been identified.

Experimental

Preparation of TNAs. Anatase TNAs were prepared by second anodic oxidation and annealing in vacuum. Prior to the oxidation, titanium foils (12×20 mm²) were polished in a mixture of hydrofluoric acid and nitric acid for 1 min (HF/HNO₃/H₂O = 1:4:5 in volume). After rinsed with DI water, the Ti foils were further cleaned by ultrasonication in acetone, ethanol and deionized (DI) water successively before drying with nitrogen stream. The first anodization of the Ti foils as anodes was carried out at 50 V DC potential in a home-made well-sealed two-electrode cell at room temperature using graphite sheets as cathodes. The electrolyte consisted of ethylene glycol containing 0.4 wt. % NH₄F and a small amount of DI water. After 2h oxidation, the first-grown inhomogeneous TNA membrane was removed by ultrasonication in DI water for several minutes, leaving a hexagonally packed pattern of regular shallow pits on the Ti foil surface. The second anodization was then performed under the same conditions as the first anodization, and the hexagonally packed pattern served as a template to guide the vertical growth of nanotubes underneath during the second oxidation. The as-grown amorphous TNAs were rinsed with DI water for several times and dried with nitrogen stream. To induce crystallization into the anatase phase, the amorphous TNAs were calcined at 450 °C for 2 h at a heating rate of 0.5 °C min⁻¹ in a CVD system. Poor-oxygen (vacuum or Ar) and rich-oxygen (air or O₂) annealing atmospheres were used to control the content of oxygen vacancies and the crystallization orientation. The growth rate and nanotube length of the arrays were tuned by varying the water content (1–4 wt %) and second oxidation time (2–8h).

Material characterization. X-ray powder diffraction (XRD) patterns were obtained with a Rigaku D/max-2200 using Cu Kα radiation. SEM images were taken with JEOL FESEM-6700F under voltage of 15 KV. TEM observations were performed on aberration-corrected TEM (FEI Titan 80-300) operating at 80 kV acceleration voltage. XPS spectra were collected using Thermo ESCALAB 250Xi X-ray photoelectron spectrometer.

Electrochemical measurements. Several batches of *c*- and *r*-TNAs on titanium foils with a diameter of 12 mm were used to made electrochemical measurements. Before the measurements, an average net weight of TiO₂ on titanium foils was weighed to determine specific capacities. The net weight of TiO₂ on titanium foils can be measured exactly with an electronic balance, because thick TNA films on titanium foils can be fully exfoliated from the Ti substrates. The exfoliated samples for the weight measurement were made by re-anodizing TNAs in ethylene glycol for 10 min at a DC potential of 50 V. After immersed into 33% H₂O₂ solution for 10 min, TNA membranes were fully detached from the Ti substrates, rinsed with alcohol and water to remove residual electrolyte and H₂O₂, and dried at 80 °C before the weight measurement. The electrochemical

measurements were carried out on Land-CT2001A battery test system at room temperature using lithium metal as the counter electrode, 1 M LiPF₆ dissolved in dimethyl carbonate (DMC), diethyl carbonate (DEC) and ethylene carbonate (EC) (1:1:1 by weight) as the electrolyte. The cells were assembled in a glove box filled with argon gas. The supercapacitor properties of TNAs (1 cm²) were investigated by cyclic voltammetry (CV) and galvanostatic charge/discharge measurements at room temperature in a conventional three-electrode H-shape cell employing the CHI 660e electrochemical workstation. An Ag/AgCl (1M KCl) electrode was used as reference electrode, and a platinum wire as counter electrode, and a 0.5 M Na₂SO₄ solution as electrolyte. Electrochemical impedance spectroscopy (EIS) of TNAs was measured using a CHI 660e electrochemical workstation with a platinum foil as counter electrode and 1M LiClO₄ in propylene carbonate as electrolyte. The data were collected from 1 to 10 MHz.

Acknowledgements

This work has been supported by National Natural Science Foundation of China (No. 91233102, 11174194, 11025526), Program for Changjiang Scholars and Innovative Research Team in University (No. IRT13078), Innovation Program of Shanghai Municipal Education Commission (No. 13YZ017, 13ZZ076), Science and Technology Commission of Shanghai Municipality (No. 13230500600), Shanghai Leading Academic Discipline Project (No. S30109), China Postdoctoral Science Foundation funded project (2012M520874), and Shanghai Postdoctoral Scientific Program (13R21413100).

Notes and references

^aInstitute of Nanochemistry and Nanobiology, Shanghai University, Shangda Road 99, Shanghai 200444, P.R. China.

^bShanghai Applied Radiation Institute, Shanghai University, Shangda Road 99, Shanghai 200444, P.R. China.

^cSchool of Environmental and Chemical Engineering, Shanghai University, Shangda Road 99, Shanghai 200444, P.R. China.

*E-mail: dypan617@shu.edu.cn; lizhen@shu.edu.cn; mhwu@shu.edu.cn.

† Electronic Supplementary Information (ESI) available: [details of any supplementary information available should be included here]. See DOI: 10.1039/b000000x/

- N.-S. Choi, Y. Yao, Y. Cui and J. Cho, *J. Mater. Chem.*, 2011, **21**, 9825.
- C. C. Hu, K. H. Chang, M. C. Lin and Y. T. Wu, *Nano Lett.*, 2006, **6**, 2690-2695.
- X. Lu, D. Zheng, T. Zhai, Z. Liu, Y. Huang, S. Xie and Y. Tong, *Energy Environ. Sci.*, 2011, **4**, 2915.
- G.-N. Zhu, Y.-G. Wang and Y.-Y. Xia, *Energy Environ. Sci.*, 2012, **5**, 6652.
- D. Deng, M. G. Kim, J. Y. Lee and J. Cho, *Energy Environ. Sci.*, 2009, **2**, 818.
- V. Gentili, S. Brutti, L. J. Hardwick, A. R. Armstrong, S. Panero and P. G. Bruce, *Chem. Mater.*, 2012, **24**, 4468-4476.
- S. Södergren, H. Siegbahn, H. Rensmo, H. Lindström, A. Hagfeldt and S.-E. Lindquist, *J. Phys. Chem. B*, 1997, **101**, 3087-3090.
- J. S. Chen, Y. L. Tan, C. M. Li, Y. L. Cheah, D. Luan, S. Madhavi, F. Y. Boey, L. A. Archer and X. W. Lou, *J. Am. Chem. Soc.*, 2010, **132**, 6124-6130.
- D. Wang, D. Choi, J. Li, Z. Yang, Z. Nie, R. Kou, D. Hu, C. Wang, L. V. Saraf, J. Zhang, I. A. Aksay and J. Liu, *ACS nano*, 2009, **3**, 907-914.
- Z. Yang, D. Choi, S. Kerisit, K. M. Rosso, D. Wang, J. Zhang, G. Graff and J. Liu, *J. Power Sources*, 2009, **192**, 588-598.
- H. Han, T. Song, E. K. Lee, A. Devadoss, Y. Jeon, J. Ha, Y. C. Chung, Y. M. Choi, Y. G. Jung and U. Paik, *ACS nano*, 2012, **6**, 8308-8315.
- S. K. Cheah, E. Perre, M. Rooth, M. Fondell, A. Harsta, L. Nyholm, M. Boman, T. Gustafsson, J. Lu, P. Simon and K. Edstrom, *Nano Lett.*, 2009, **9**, 3230-3233.
- S. Dong, H. Wang, L. Gu, X. Zhou, Z. Liu, P. Han, Y. Wang, X. Chen, G. Cui and L. Chen, *Thin Solid Films*, 2011, **519**, 5978-5982.
- D. Liu, Y. Zhang, P. Xiao, B. B. Garcia, Q. Zhang, X. Zhou, Y.-H. Jeong and G. Cao, *Electrochim. Acta*, 2009, **54**, 6816-6820.
- D. Fang, K. Huang, S. Liu and Z. Li, *J. Alloys Compd.*, 2008, **464**, L5-L9.
- G. F. Ortiz, I. Hanzu, T. Djenizian, P. Lavela, J. L. Tirado and P. Knauth, *Chem. Mater.*, 2009, **21**, 63-67.
- Q. L. Wu, J. Li, R. D. Deshpande, N. Subramanian, S. E. Rankin, F. Yang and Y.-T. Cheng, *J. Phys. Chem. C*, 2012, **116**, 18669-18677.
- J. R. González, R. Alcántara, F. Nacimiento, G. F. Ortiz, J. L. Tirado, E. Zhecheva and R. Stoyanova, *J. Phys. Chem. C*, 2012, **116**, 20182-20190.
- Z. Yang, D. Pan, C. Xi, J. Li, J. Shi, F. Xu and Z. Ma, *J. Power Sources*, 2013, **236**, 10-16.
- K. Shankar, G. K. Mor, H. E. Prakasam, S. Yoriya, M. Paulose, O. K. Varghese and C. A. Grimes, *Nanotechnology*, 2007, **18**, 065707.
- L. Shen, E. Uchaker, X. Zhang, G. Cao, *Adv. Mater.*, 2012, **24**, 6502-6506.
- J. R. Jennings, A. Ghicov, L. M. Peter, P. Schmuki and A. B. Walker, *J. Am. Chem. Soc.*, 2008, **130**, 13364-13372.
- G. K. Mor, O. K. Varghese, M. Paulose, K. Shankar and C. A. Grimes, *Sol. Energy Mater. Sol. Cells*, 2006, **90**, 2011-2075.
- X. Lu, G. Wang, T. Zhai, M. Yu, J. Gan, Y. Tong and Y. Li, *Nano Lett.*, 2012, **12**, 1690-1696.
- M. Salari, S. H. Aboutalebi, K. Konstantinov and H. K. Liu, *Phys. Chem. Chem. Phys.*, 2011, **13**, 5038-5041.
- Y. Xie and D. Fu, *Mater. Res. Bull.*, 2010, **45**, 628-635.
- M. S. Kim, T.-W. Lee and J. H. Park, *J. Electrochem. Soc.*, 2009, **156**, A584.
- M. Salari, K. Konstantinov and H. K. Liu, *J. Mater. Chem.*, 2011, **21**, 5128.
- D. Wang, L. Liu, F. Zhang, K. Tao, E. Pippel and K. Domen, *Nano Lett.*, 2011, **11**, 3649-3655.
- S. Berger, J. Kunze, P. Schmuki, A. T. Valota, D. J. LeClere, P. Skeldon and G. E. Thompson, *J. Electrochem. Soc.*, 2010, **157**, C18.
- J. M. Macak, H. Tsuchiya and P. Schmuki, *Angew. Chem. Int. Ed. Engl.*, 2005, **44**, 2100-2102.
- C. R. Fell, D. Qian, K. J. Carroll, M. Chi, J. L. Jones and Y. S. Meng, *Chem. Mater.*, 2013, **25**, 1621-1629.

33. N. Yabuuchi, K. Yoshii, S. T. Myung, I. Nakai and S. Komaba, *J. Am. Chem. Soc.*, 2011, **133**, 4404-4419.
34. F. Fabregat-Santiago, E. M. Barea, J. Bisquert, G. K. Mor, K. Shankar and C. A. Grimes, *J. Am. Chem. Soc.*, 2008, **130**, 11312-11316.